

CHEMICAL PHYSICS

Inward growth by nucleation: Multiscale self-assembly of ordered membranes

Jasper Landman^{1,2,3}, Samia Ouhajji¹, Sylvain Prévost⁴, Theyencheri Narayanan², Jan Groenewold^{1,5}, Albert P. Philipse¹, Willem K. Kegels¹, Andrei V. Petukhov^{1,3*}

Striking morphological similarities found between superstructures of a wide variety of seemingly unrelated crystalline membrane systems hint at the existence of a common formation mechanism. Resembling systems such as multiwalled carbon nanotubes, bacterial protein shells, or peptide nanotubes, the self-assembly of SDS/ β -cyclodextrin complexes leads to monodisperse multilamellar microtubes. We uncover the mechanism of this hierarchical self-assembly process by time-resolved small- and ultrasmall-angle x-ray scattering. In particular, we show that symmetric crystalline bilayers bend into hollow cylinders as a consequence of membrane line tension and an anisotropic elastic modulus. Starting from single-walled microtubes, successive nucleation of new cylinders inside preexisting ones drives an inward growth. As both the driving forces that underlie the self-assembly behavior and the resulting morphologies are common to systems of ordered membranes, we believe that this formation mechanism has a similarly general applicability.

INTRODUCTION

The superstructures that occur in self-assemblies of crystalline membranes often share a set of common morphologies: They form hollow shells, single- or multiwalled (nano)tubes, or lamellae. Single- and multiwalled (nano)tubes are found in self-assemblies of amphiphilic peptides (1–3) and the allotropes of carbon (4–8). The same morphologies are also found in living systems such as microtubuli (9–11), bacterial protein shells (12), and bacterial chlorosomes (13–15). The striking morphological similarities between these seemingly unrelated systems suggest that the driving forces underlying their self-assembly mechanisms are common to many of these systems, depending more on the interplay between rigidity and the high energy cost of membrane edges than on the nanoscopic details of the individual systems. Moreover, these types of system often share a remarkable degree of monodispersity. Hence, this suggests the existence of a well-defined formation mechanism, common to a broad range of systems of crystalline membranes.

The self-assembly of sodium dodecyl sulfate (SDS) and β -cyclodextrin (β -CD) leads to superstructures that are representative of the class of crystalline membrane materials. In the work of Jiang *et al.* (16–18) and Yang *et al.* (19), the rich phase behavior of the SDS/ β -CD system was explored, showing, among others, multiwalled microtubes, polyhedral capsids, and lamellar phases, as shown in Fig. 1. A common feature of all these superstructures is a rigid crystalline bilayer membrane, with a well-ordered internal structure that is identical regardless of the higher-order organization.

In our previous work (20), we demonstrated the use of small- and ultrasmall-angle x-ray scattering (SAXS and USAXS, respectively) to determine the structure of SDS/ β -CD microtubes *in situ*. From the scattering profiles, we were able to quantify microtube radii and inter- and intrabilayer periodicities from the scattering profiles at low, intermediate, and high q , respectively. By measuring the small-angle scattering profiles, we essentially have access to structural information

on multiple length scales, opening the door to detailed mechanistic studies of self-assembly processes. Here, we follow the kinetics of SDS/ β -CD structure formation, using time-resolved SAXS. From the resulting structural information, we uncover the mechanism of microtube self-assembly.

RESULTS

Kinetic measurements

We obtained USAXS patterns of temperature-quenched solutions of [SDS@2 β -CD] in the process of self-assembly on the USAXS beamline ID02 at the European Synchrotron Radiation Facility (ESRF). The technique was previously used to follow the self-assembly kinetics of various systems, such as virus capsids (21, 22). In a typical experiment, a heated, premade solution of [SDS@2 β -CD] was injected in an observation capillary kept at room temperature, effecting a rapid temperature jump. Immediately after injection, SAXS patterns were recorded in regular, increasing intervals. Figure 2 shows the azimuthally averaged SAXS profiles of a typical experiment as a function of time after injection. The initial SAXS intensities correspond to the form factor of the [SDS@2 β -CD] complex in solution, which is formed as the hydrophobic tail of the SDS molecule is inserted into the hydrophobic pocket of two β -CD molecules. The data show an initial waiting time before the scattering profile visibly changes. After this initial waiting time, which we denote as t_0 , there is a significant increase in scattering at small angles. Simultaneously, peaks appear at higher angles, corresponding to the in-plane organization of the [SDS@2 β -CD] complexes. These peaks do not shift during the course of an experiment, a confirmation that the in-plane organization of [SDS@2 β -CD] complexes is unchanged throughout the self-assembly process.

Initial formation of cylinders

During the increase in scattering intensity, oscillations are visible at small angles: Up to 20 orders can be observed during these intermediate stages of the self-assembly. The oscillations appear throughout our experiments, although they are clearest in samples when the [SDS@2 β -CD] concentration is around 6 to 10 wt %. The oscillations only dampen out after a large number of orders. This indicates that the structure present in the sample is highly monodisperse, with a standard deviation (SD) in the average radius well below 5%. We plot a subset of the

Copyright © 2018
The Authors, some
rights reserved;
exclusive licensee
American Association
for the Advancement
of Science. No claim to
original U.S. Government
Works. Distributed
under a Creative
Commons Attribution
NonCommercial
License 4.0 (CC BY-NC).

¹Van 't Hoff Laboratory for Physical & Colloid Chemistry, 3584 CH Utrecht, Netherlands.

²European Synchrotron Radiation Facility, 38000 Grenoble, France. ³Laboratory of Physical Chemistry, Eindhoven University of Technology, 5600 MB Eindhoven, Netherlands. ⁴Institut Laue-Langevin, 38000 Grenoble, France. ⁵Guangdong Provincial Key Laboratory of Optical Information Materials and Technology and Institute of Electronic Paper Displays, South China Normal University, Guangzhou 510006, P. R. China.

*Corresponding author. Email: a.v.petukhov@uu.nl

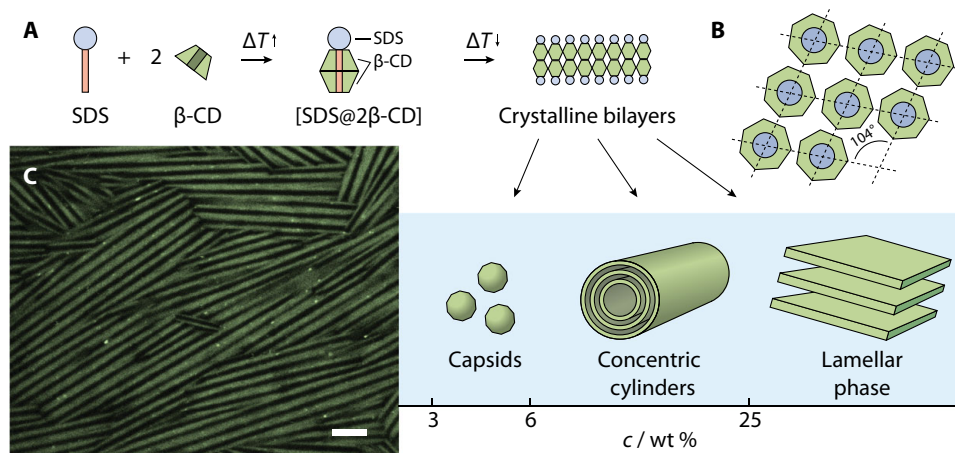


Fig. 1. Self-assembly of β -CD and SDS into concentric hollow microtubes, lamellar phases, or polyhedral capsids. (A) In solution, the hydrophobic tail of the SDS molecule will preferentially reside in the hydrophobic pocket of two stacked β -CD molecules, creating a compact unit, the $[\text{SDS}@2\beta\text{-CD}]$ complex (16). Above 40°C , the complexes are soluble in water. Below this temperature, the complexes spontaneously form bilayers that self-assemble into polyhedral capsids, multiwalled microtubes, or lamellar phases depending on the concentration. Below 3 weight % (wt %), no superstructures are observed. The process is thermoreversible, as discussed in the Supplementary Materials. Above the melting temperature, the structures disassemble back into the individual complexes (16–18). (B) Yang *et al.* (19) showed that the complexes are organized in-plane in a rhombic lattice, showing that the formation of these rhombic bilayers is a logical consequence of the sevenfold symmetry of the β -CD molecule. The structure optimizes the alignment of in-plane hydrogen bonds between the cyclodextrins. (C) Confocal microscopy image of $[\text{SDS}@2\beta\text{-CD}]$ microtubes, stained with Nile red fluorescent dye. Scale bar, $5\ \mu\text{m}$.

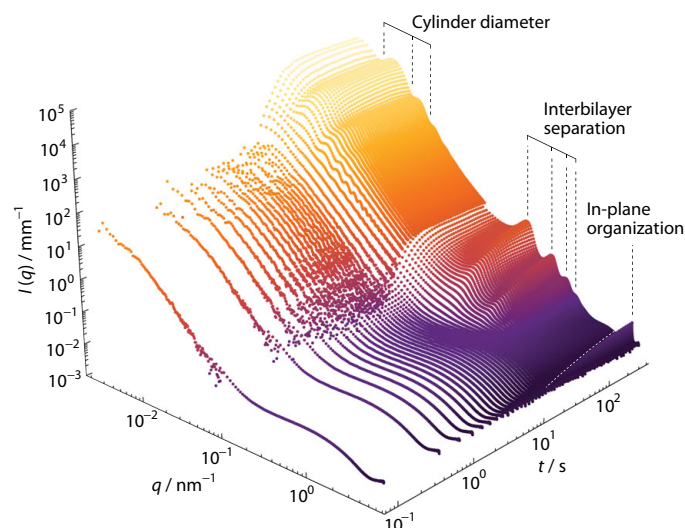


Fig. 2. Time evolution of SAXS profiles. A 10 wt % hot solution of $[\text{SDS}@2\beta\text{-CD}]$ was rapidly quenched to room temperature. Intensity is plotted as a function of scattering vector $q = \frac{4\pi}{\lambda} \sin \frac{\theta}{2}$, where λ is the wavelength of the incident x-rays and θ as the scattering angle. The initial scattering intensity corresponds to the form factor of the $[\text{SDS}@2\beta\text{-CD}]$ complex in solution. After an initial waiting time, the structure almost simultaneously appears at all length scales. Data from two sample-to-detector distances were appended and partially binned to average out the noisy tail of the low- q measurements at the start of the experiment.

SAXS profiles of the experiment, with one curve highlighted showing pronounced oscillations, in Fig. 3. The scattering intensity follows an inverse square decay, the expected scaling for a two-dimensional (2D) object. Moreover, the profile closely resembles the theoretical form factor of hollow cylinders (23).

The intermediate structures observed in Fig. 3A are extremely monodisperse, which is surprising, because symmetrical bilayers are

expected to have zero preferential curvature. It is likely that the edges of $[\text{SDS}@2\beta\text{-CD}]$ bilayers are highly unstable, an indication of which is given by the very low solubility of β -CD in comparison to other cyclodextrins (24). Hence, the energy cost of bending the bilayer into a cylindrical geometry is compensated by the large gain in bond free energy provided upon closure of the cylinder. Competition between bond formation and bending free energy leads to a minimum in the free energy per complex, which we show in fig. S3. A similar mechanism has been observed in the formation of monodisperse spherical vesicles from fluid membranes (25, 26). We provide arguments in the Supplementary Materials that support a preference for a cylindrical geometry in crystalline membranes.

Microtube radius and inward growth

We show the azimuthally integrated SAXS profiles of a typical experiment in Fig. 3C. The profiles were fitted to the form factor of long hollow cylinders with a central radius $\langle r \rangle$ and a thickness $\langle \delta \rangle$, given by the equation (23, 27)

$$I(q) = \frac{2\pi^3 l}{q} \left[\frac{(r + \frac{\delta}{2}) J_1(q(r + \frac{\delta}{2}))}{q} - \frac{(r - \frac{\delta}{2}) J_1(q(r - \frac{\delta}{2}))}{q} \right]^2 \quad (1)$$

where l is the total length of the cylinders and J_1 is the Bessel function of the first kind. While the equation is an approximation, we show in the Supplementary Materials that it provides good approximations for the mean radius and multilamellar stack thickness even when the cylinder length and radius are comparable. The resulting radii and thicknesses are plotted as a function of time in Fig. 3D. For comparison, we plot the Porod invariant $Q = \int q^2 \times I(q) dq$ (28), a measure for the amount of ordered material present at each point in time during the self-assembly process, in Fig. 3E. The average central radius $\langle r \rangle$ initially decreases rapidly, followed by a stabilization at longer time scales. Our fits show a concurrent increase in the cylinder thickness $\langle \delta \rangle$, consistent with a constant outer radius equal to $r_0 = \langle r \rangle + \langle \delta \rangle / 2$. Hence, we attribute this effect to an inward growth process. If the growth is directed inward, then the

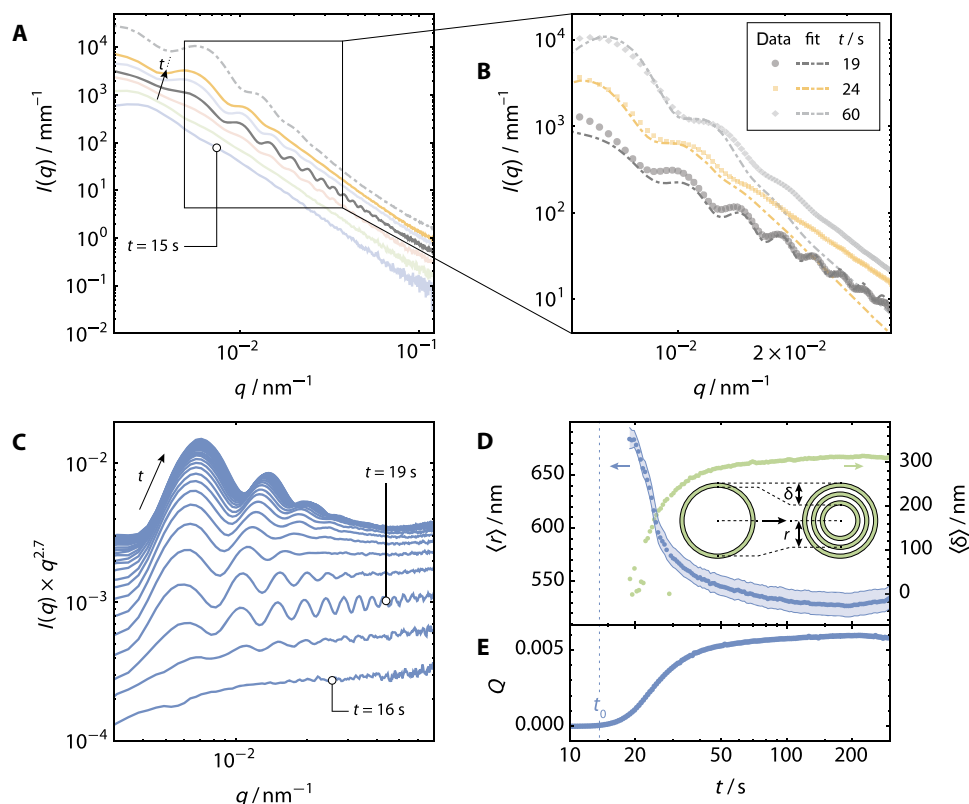


Fig. 3. Ultrasmall-angle scattering experiments. (A) SAXS profiles of a subset of a typical experiment, showing the many oscillations in the intermediate states of self-assembly, together with a profile during the later stages of self-assembly. Even before the emergence of oscillations, the scattering profiles show a slope at very small angles, indicating large-scale density fluctuations. (B) Fits of selected SAXS profiles to a model of hollow cylinders (23). The shallow amplitude is likely caused by a convolution with the detector point-spread function, combined with a comparatively short but highly polydisperse cylinder length. (C) Integrated SAXS profiles multiplied by a power of q , showing the appearance and shift of oscillations due to the radius of the microtubes. (D) Average cylinder radius $\langle r \rangle$ and thickness $\langle \delta \rangle$ from fits to the simplified expression in Eq. 1. To aid the fit, the average radius of the previous five profiles was given as the starting point for the fit of each successive curve. The shaded area denotes the extent of the 95% confidence interval. (E) Time evolution of the Porod invariant Q , for comparison. The Porod invariant was calculated by integration over the accessible q range only.

outer radius of the microtubes should remain constant throughout an experiment, which is confirmed by the observed positions of the scattering minima at low q ($\sim 0.005 \text{ nm}^{-1}$) in Fig. 2 and in optical microscopy observations shown in fig. S1.

The experiment was repeated for a number of different [SDS@2 β -CD] concentrations. The resulting evolutions of the average central radius $\langle r \rangle$ are plotted in Fig. 4A. All experiments show a similar decrease in average radius. The slight increase of average radius at the end of the experiment likely reflects a separate relaxation process that is independent of concentration. Most probably, this effect is caused by convective processes within the scattering cell.

The presence of a concentration-dependent initial waiting time is reminiscent of a nucleation process. Classical nucleation theory was introduced in the 1920s and 1930s (29–31) as a means to model the homogeneous nucleation rate of a supersaturated solution in microscopic terms. Within the framework, the nucleation rate depends on the concentration in a highly nonlinear way, depending on the dimensionality of a critical nucleus. For a disc-shaped 2D critical nucleus, the nucleation rate follows an Arrhenius-type equation, given by

$$j = A \exp\left(-\frac{\pi\tau^2 a_0}{k_B T |\Delta\mu|}\right) = A \exp\left(-\frac{\pi\tau^2 a_0}{(k_B T)^2 \log \frac{c}{c^*}}\right) \quad (2)$$

where j is the nucleation rate within the observed volume, τ is the microscopic line tension of the edge of the disc, a_0 is the molecular surface area occupied by a single [SDS@2 β -CD] complex, and A is a kinetic prefactor. The chemical potential $\Delta\mu = -k_B T \log S$ is a function of the degree of supersaturation $S = c/c^*$, where c is the concentration of [SDS@2 β -CD] complexes and c^* is the saturation concentration, which we estimate at 3 wt % (see Fig. 1). A derivation of the equation for a disc-shaped critical nucleus is presented in the Supplementary Materials. If we take the reciprocal of the nucleation rate as a typical nucleation time scale, $t_0 \sim j^{-1}$, then the theory predicts that the logarithm of the typical nucleation time scale should be inversely proportional to the logarithm of the degree of supersaturation, with an intercept determined by the preexponential factor A . We plot the logarithm of the initial waiting time, $\log t_0$, as a function of $(\log \frac{c}{c^*})^{-1}$ in Fig. 4B. The data are convincingly described by a linear function. From the extrapolated intercept, we determined the preexponential factor to be $A = 1.5 \text{ s}^{-1}$. Moreover, if we rescale the time axis of the experiments in Fig. 4A and plot the evolution of the average central radius $\langle r \rangle$ as a function of $\log t A \times \log c/c^*$ in Fig. 4C, then the data from all experiments collapse onto a single curve: The full kinetics of inward growth show classical nucleation scaling with concentration.

The mechanism of microtubule formation can therefore be understood as illustrated in Fig. 5. Complexes of [SDS@2 β -CD] in a supersaturated solution (Fig. 5A) nucleate into critical (2D) nuclei (Fig. 5B),

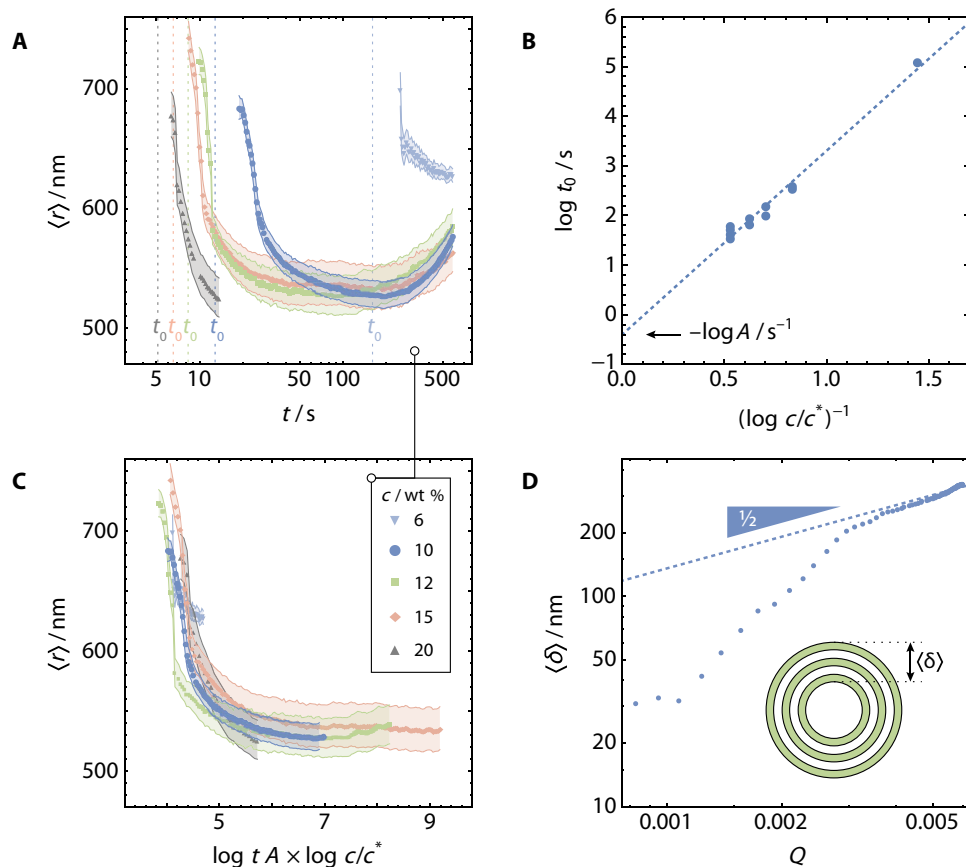


Fig. 4. Inward growth is a nucleation process. (A) Time evolution of the average central microtube radius $\langle r \rangle$ for different [SDS@2 β -CD] concentrations. (B) The logarithm of t_0/s scales linearly with the reciprocal of the logarithm of c/c^* , as predicted by classical nucleation theory for a disc-shaped critical nucleus. Moreover, when the average microtube radius is plotted in (C) as a function of $\log t A \times \log c/c^*$, all the data collapse onto a single curve. (D) The thickness $\langle \delta \rangle$ of the (multi-)wall shows a typical square-root scaling with the Porod invariant Q over the later part of the experiment. The shaded areas in (A) and (C) denote the extent of the 95% confidence intervals.

which grow into bilayers. When a bilayer reaches a size large enough that the bending free energy can be overcome, cylinder closure occurs (Fig. 5C). The minimum in free energy, arising from a competition between bending free energy and bond free energy, leads to a population of monodisperse, single-walled cylinders. Cylinder closure occurs while the process of nucleation continues, and critical nuclei are formed on both the inside and outside of existing cylinders (Fig. 5D). Sheets formed within the cylinders are confined and can only form cylinders that are slightly smaller than their preferred size (Fig. 5E). Successive nucleation on the inside of existing cylinders causes the formation of a stack of concentric cylinders. Nucleation of new cylinders on the outside of existing cylinders occurs until the volume is closely packed (Fig. 5F). It is likely that the outer layers are deformed due to packing effects, causing the decay of the higher-order oscillations that are so apparent in the intermediate stages of the self-assembly process (27).

Within this mechanism, the growth of individual bilayers is constrained. Bonds with neighboring complexes occur only within the plane of the bilayer, and consequently, growth in thickness only occurs by nucleation of a new bilayer to form a stack. The width of a bilayer grows until cylinder closure occurs, and additional growth also has to occur by nucleation of new bilayers. In length, growth is constrained by the presence of other microtubes. Macroscopic growth can therefore only occur in width or in thickness, both exhibiting nucleation kinetics.

Hence, the average microtube thickness should scale with the square root of the total amount of bilayers. We plot the average cylinder thickness $\langle \delta \rangle$, calculated from the shift in $\langle r \rangle$, as a function of the Porod invariant (Q) in Fig. 4D. Over the most part of the experiment, the thickness of the stack of bilayers scales with the square root of Q and thus with the amount of structured material.

At the start of the experiment, the growth in thickness is faster than the typical square root scaling, most likely due to the presence of nucleated bilayers in which cylinder closure has not occurred yet. These bilayers do contribute to the invariant Q . While we have no structural probe to detect flat membranes in the same experiment, there is evidence that the [SDS@2 β -CD] bilayers go through a flat intermediate stage: Yang *et al.* (19) observed thin, diamond-shaped sheets with an obtuse angle of 104°, identical to the obtuse angle of the rhombic bilayer lattice, as a minority product in self-assembled microtubes of [SDS@2 β -CD] complexes. We speculate that a small fraction of bilayers has insufficient space available for cylinder closure, which can then be observed in the final structure by microscopy.

Interbilayer separation

Up to now, we did not consider the magnitude of the inward growth process. This magnitude is related to the typical spacing between successive concentric tubes. We traced the average spacing between

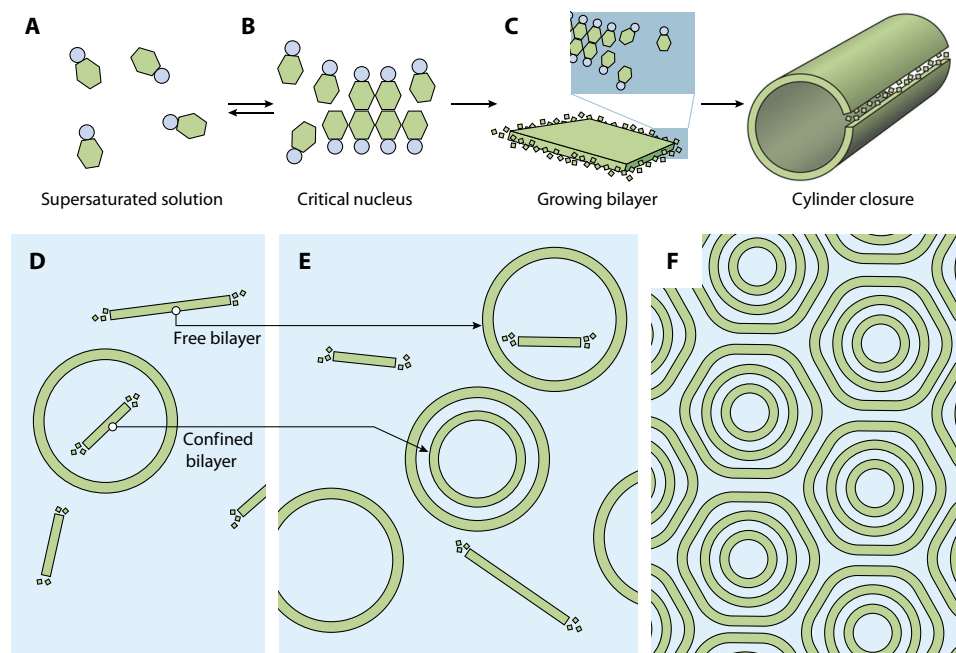


Fig. 5. Proposed mechanism for the microtube formation. (A) [SDS@2β-CD] complexes in solution nucleate into (B) ordered bilayers, governed by directional hydrogen bonding with their neighbors. (C) When the bilayer reaches a certain size, it becomes advantageous to close the ring, gaining bond free energy at the cost of bending free energy. (D) Because nucleation and growth are not separated, new bilayers keep nucleating, both inside and outside preexisting tubes. (E) Bilayers that nucleated outside preexisting tubes form new tubes. Bilayers that nucleated inside preexisting tubes are restricted in their size and form concentric inner cylinders. (F) Because of the large amount of material that is accommodated in the bilayers in a limited space, a dense packing of concentric cylinders is obtained. The cylinders are consequently deformed in a slightly hexagonal form (27). Evidence for this deformation is given in fig. S2.

multiple bilayers from the periodicity of the peaks present at intermediate angles. We show azimuthally integrated SAXS profiles of a typical experiment, multiplied by q^2 to decouple the bilayer structure factor from the cylinder form factor with apparent q^{-2} decay, in Fig. 6A. The maxima of the peaks were consequently found by cubic interpolation and are shown superimposed on the scattering profiles in Fig. 6A. As the amount of ordered material increases, the average spacing $\langle d \rangle$ increases slightly over time, as we show in Fig. 6 (B and C).

The interbilayer separation can be understood as a competition between electrical double-layer repulsion between charged interfaces and the increased energy cost of bending the [SDS@2β-CD] membranes into tighter cylinders (32–34). The electrical double-layer repulsion is affected by the salt in the system; however, addition of up to 10^{-3} M NaCl has no measurable impact on the interbilayer separation, as shown in the Supplementary Materials. Likely, a fraction of [SDS@2β-CD] complexes is not incorporated in bilayers but acts as an additional salt reservoir. The increase in interbilayer separation visible in Fig. 6B is then likely caused by lower screening, as more [SDS@2β-CD] complexes are incorporated in bilayers.

The final interbilayer separation is concentration-dependent. We measured the SAXS patterns of a concentration series of preassembled [SDS@2β-CD] samples on the Dutch-Belgian Beamline (DUBBLE) at the ESRF, as shown in Fig. 6D. We determined the average interbilayer separation from the average peak separation, which we plot as a function of concentration in Fig. 6E. For samples of a concentration above 25 wt %, the interbilayer separation scales with the reciprocal of the concentration, expected for a purely lamellar phase. In the concentration regime where microtubes occur, the scaling is sublinear, reflecting the more compacted structure with open central pores in each microtube.

We put forward a model to explain the observed concentration scaling based on Helfrich's expression for the bending free energy of membranes (35). We derived an expression for the average bending free energy per unit interface \bar{f} bend for a set of concentric cylinders, which to a first-order approximation reads

$$\bar{f} \approx \frac{\kappa}{2r_0^2} + \frac{\kappa}{2r_0^2} \frac{\sqrt{3}ca_0d}{2\pi} + \dots \quad (3)$$

where κ is the mean elastic modulus of the membrane, r_0 is the radius of the outermost cylinder, a_0 is the interfacial area occupied by a single [SDS@2β-CD] complex, c is the number density of [SDS@2β-CD] complexes, and d is the interbilayer separation. A full derivation of this expression is given in the Supplementary Materials. For interbilayer separations comparable to the Debye length, the weak overlap Debye-Hückel approximation is not very accurate. Instead, we use the expression for disjoining pressure due to electrical double-layer repulsion, derived by Philipse *et al.* (36, 37) for a system of parallel plates with extensive double-layer overlap. The electrical free energy per unit interface is given within this framework as

$$f_{\text{el}} = \frac{k_B T \sigma^2}{\rho_s} \frac{1}{d} \quad (4)$$

where σ is the surface charge number density of the membrane and ρ_s is the salt number density. The interbilayer spacing that optimizes the total free energy is then found by taking the partial derivative of f with

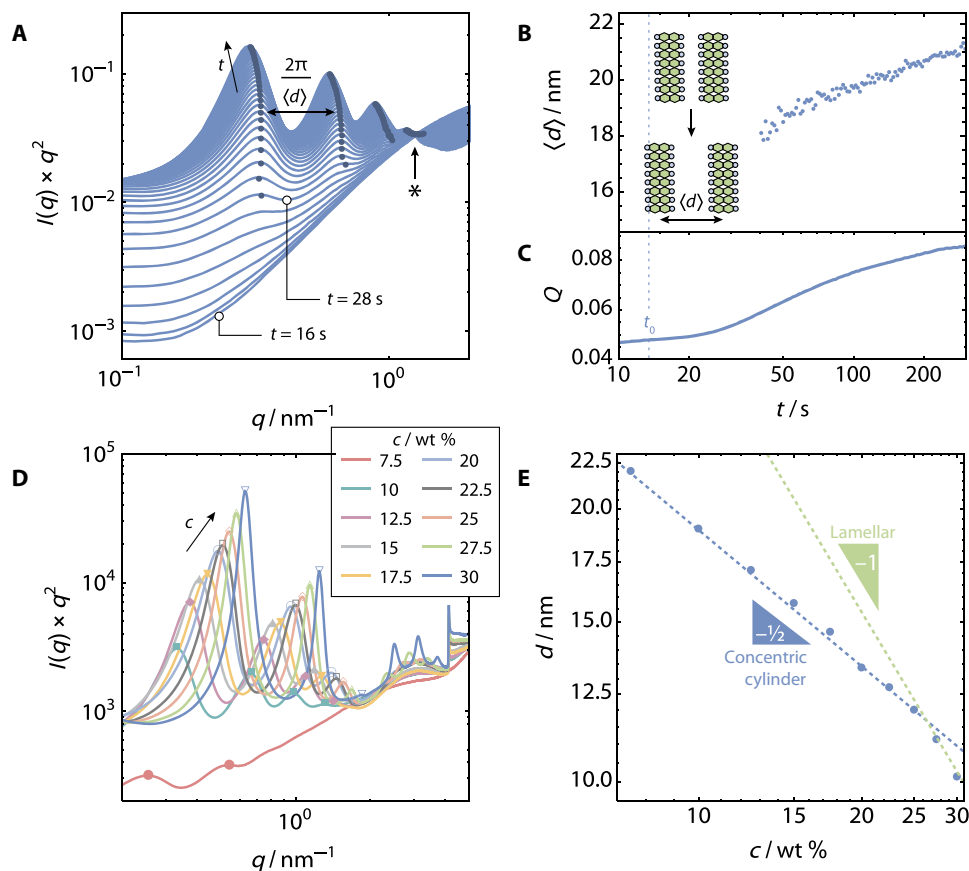


Fig. 6. Tracing the interbilayer separation. (A) Integrated SAXS profiles recorded after temperature quench, multiplied by a power of q to compensate for the apparent q^{-2} decay. The asterisk denotes the presence of an iso-scattering point. Time evolution of (B) the average spacing $\langle d \rangle$ calculated from the peak positions in (A), and (C) the Porod invariant Q , given by integrating $I(q) \times q^2$ over the full q range. The Porod invariant is proportional to the amount of (structured) material (28). The spacing between the bilayers appears first at approximately 18 nm and shifts slowly to higher values. In the final sample, on the order of 10 concentric cylinders are present. (D) Static SAXS profiles of preassembled [SDS@2 β -CD] complexes. When plotted as a function of concentration in (E), the interbilayer distance $\langle d \rangle$ scales with the expected c^{-1} in the concentration regime where the structure is lamellar. In the tubular concentration regime, the interbilayer spacing scales with $1/\sqrt{c}$.

respect to d and setting it to zero. We found that the optimal interbilayer spacing d^* is given by

$$d^* = \sqrt{\frac{k_B T \sigma^2}{\rho_s} \frac{4\pi r_0^2}{\sqrt{3} a_0 \kappa c}} \propto \frac{1}{\sqrt{c}} \quad (5)$$

The predicted $1/\sqrt{c}$ scaling matches convincingly with the experimentally observed concentration dependence. There are three free parameters: κ , σ , and ρ_s . We estimate the bulk salt concentration ρ_s to be approximately 10^{-3} M from the results of the experiment shown in fig. S5. The mean elastic modulus κ and surface charge density σ cannot be determined independently from this experiment. Double-layer lipid membranes typically have mean elastic moduli on the order of $10^2 k_B T$, and we estimate that the [SDS@2 β -CD] bilayers are somewhat stiffer due to their high degree of order. If we estimate κ to be on the order of $100 k_B T$, then we find from the resulting surface charge density that a large fraction of counterions are condensed, leaving approximately 0.15% of all [SDS@2 β -CD] complexes in the bilayers charged. While the weak-field approach of Philipse *et al.* (36) was shown to match accurately with numerical solutions of the Poisson-Boltzmann equation, to our knowledge, this is the first quantitative demonstration of the predicted $1/d$ scaling in an experimental system.

DISCUSSION

We measured the kinetics of the hierarchical self-assembly of SDS and β -CD into multiwalled microtubes using time-resolved (U)SAXS after a rapid temperature quench. The [SDS@2 β -CD] complexes in solution were found to nucleate into highly ordered, rhombic bilayers that close into cylinders when reaching a sufficiently large size. The cylindrical geometry is likely an effect of an anisotropic elastic modulus, as indicated by the correlation between the alignment of the planar, rhombic [SDS@2 β -CD] lattice and the overall microtube direction.

The nucleation process follows the kinetics of classical nucleation. The observed inward growth of the microtubes is caused by successive nucleation of new [SDS@2 β -CD] bilayers inside existing cylinders, until a densely packed system of concentric cylinders is obtained. The interbilayer separation was found to be determined by a competition between electrical double-layer repulsion forces and the (increased) energy penalty of bending the [SDS@2 β -CD] membranes into tighter cylinders. We found that the optimal interbilayer separation scales with the inverse square root of the concentration, which is confirmed by static SAXS experiments on preassembled systems of [SDS@2 β -CD] microtubes.

In general, we argue that the driving forces that cause the formation of the elaborate microtubes do not depend on the specific chemistry of the molecular species involved. Instead, the mesoscopic behavior is a

direct consequence of three “ingredients”: the (anisotropic) bending rigidity of ordered membranes, a repulsion between the faces of the membranes, and an interfacial tension at the edges of the membrane. It is likely that the mechanism presented here has a far greater applicability than within this particular system, for example, in the behavior of biological crystalline membranes, where all three ingredients are present. In the case of carbon allotropes, the dominant repulsive contribution is of much shorter range, and the interlayer separation is determined more by the discrete nature of the lattice. However, even with that caveat, the overall morphology is strongly influenced by the bending rigidity and the high energy of dangling edge bonds, and as such, we believe that a similar mechanism may be applicable to the nucleation of carbon nanotubes in the absence of a heterogeneous catalyst.

MATERIALS AND METHODS

Solutions of [SDS@2 β -CD] inclusion complexes

Desired amounts of SDS (>99%; Sigma-Aldrich) and β -CD (97%; Sigma-Aldrich) were weighed and mixed with ultrapure water (Milli-Q), keeping a constant β -CD to SDS ratio of 2:1. The samples were heated to 75°C, yielding clear solutions. The samples were allowed to cool down to room temperature, resulting in a turbid and viscous suspension.

Confocal laser scanning microscopy

Samples were dyed by mixing 10 μ l of a solution of Nile red (1 mg ml⁻¹) (>98%; Sigma-Aldrich) in acetone with a sample at 60°C and allowing the acetone to evaporate. Observation samples were prepared by sandwiching a droplet of dyed suspension between glass coverslips (0.17 mm; Menzel Gläser). Images were recorded on a Nikon TE2000U inverted microscope with C1 confocal scan head and a 100 \times Nikon oil objective, with a 543.5-nm HeNe laser (Melles Griot) as an excitation source.

Small-angle x-ray scattering

SAXS patterns were recorded at the high-brilliance beamline ID02 (kinetic measurements) and the DUBBLE BM-26B (concentration series) at the ESRF (38, 39). For the kinetic measurements, we used two different sample-to-detector distances to cover the q range needed in our experiments. Data were recorded using a Rayonix MX170-HS detector, placed at 30.7 m for the smallest angles and at 2.5 m for the larger angles. The setup allowed measurement of scattering profiles from $q = 0.0015$ to 5 nm⁻¹, where $q = \frac{4\pi}{\lambda} \sin \frac{\theta}{2}$, where θ is the angle between incident and scattered x-rays. For the concentration series, scattering data were recorded using a Pilatus 1M detector at 1.5 m. For all measurements, background corrections were performed on all radial intensity profiles. A background measurement of pure water was obtained before each experiment. In all experiments, the x-ray wavelength was $\lambda = 0.1$ nm.

Kinetic measurements

A BioLogic SFM400 Stopped-Flow mixing device was used in the kinetic measurements to effect a fast (~ ms) temperature jump. The SFM400 was equipped with four syringes in the main reservoir. The setup and data acquisition scheme are described in more detail by Narayanan *et al.* (40). Heated samples (75°C) were loaded in one of the syringes, and the others were filled with ultrapure water. The reservoir was kept at 60° or 75°C (for 20 wt % samples). The syringes and mixers were coupled to a thermostated quartz 1.5-mm-diameter observation capillary, kept at room temperature, and placed in the path of the x-ray beam at the

ID02 beamline. In a typical experiment, the observation capillary was flushed with ultrapure water and a background measurement was obtained. The triggered release of 200 μ l of sample into the observation capillary was followed by the time-resolved recording of the SAXS patterns. Time between measurements started at 8 ms and was increased by a factor of 1.02 for each measurement. A hard stop in the outlet of the capillary was activated before the first measurement to prevent continuous flow and to dampen any remnant flows from the injection. The observation volume is sufficiently small that the temperature quench occurs in a matter of milliseconds. This was verified by the absolute scattering level of water in the compressibility limit, which is sensitive to changes in the temperature. Within the time resolution of the setup, no signature of an elevated temperature was detected after the injection of hot water. Assuming that the heat transfer and thermal capacity of the SDS/ β -CD solution are of the same order of magnitude, the temperature jump should be similarly fast.

The waiting time t_0 was defined as the point where the Porod invariant Q visibly starts to increase. To prevent bias, we estimated the waiting times from a number of different experimental sets before plotting in Fig. 4B.

SUPPLEMENTARY MATERIALS

Supplementary material for this article is available at <http://advances.sciencemag.org/cgi/content/full/4/6/eaat1817/DC1>

Supplementary Text

fig. S1. Optical microscopy during self-assembly.

fig. S2. Melting of microtubes follows reverse process.

fig. S3. Competition between bond formation and bending energy.

fig. S4. Chiral pitch of cylinders.

fig. S5. Influence of salt on the interbilayer separation.

fig. S6. Form factor fitting.

Reference (41)

REFERENCES AND NOTES

- M. Kogiso, S. Ohnishi, K. Yase, M. Masuda, T. Shimizu, Dicarboxylic oligopeptide bolaamphiphiles: Proton-triggered self-assembly of microtubes with loose solid surfaces. *Langmuir* **14**, 4978–4986 (1998).
- M. Kogiso, Y. Okada, T. Hanada, K. Yase, T. Shimizu, Self-assembled peptide fibers from valylvaline bola-amphiphiles by a parallel β -sheet network. *Biochim. Biophys. Acta* **1475**, 346–352 (2000).
- C. H. Görbitz, The structure of nanotubes formed by diphenylalanine, the core recognition motif of Alzheimer's β -amyloid polypeptide. *Chem. Commun.* 2332–2334 (2006).
- H. W. Kroto, J. R. Heath, S. C. O'Brien, R. F. Curl, R. E. Smalley, C₆₀: Buckminsterfullerene. *Nature* **318**, 162–163 (1985).
- S. Iijima, Helical microtubules of graphitic carbon. *Nature* **354**, 56–58 (1991).
- M. S. Dresselhaus, G. Dresselhaus, P. C. Eklund, A. M. Rao, in *The Physics of Fullerene-Based and Fullerene-Related Materials*, W. Andreoni, Ed. (Springer, 2000), pp. 331–379.
- K. S. Novoselov, A. K. Geim, S. V. Morozov, D. Jiang, Y. Zhang, S. V. Dubonos, I. V. Grigorieva, A. A. Firsov, Electric field effect in atomically thin carbon films. *Science* **306**, 666–669 (2004).
- A. J. Page, F. Ding, S. Irlé, K. Morokuma, Insights into carbon nanotube and graphene formation mechanisms from molecular simulations: A review. *Rep. Prog. Phys.* **78**, 036501 (2015).
- C. Valéry, M. Paternostre, B. Robert, T. Gulik-Krzywicki, T. Narayanan, J.-C. Dedieu, G. Keller, M.-L. Torres, R. Cherif-Cheikh, P. Calvo, F. Artzner, Biomimetic organization: Octapeptide self-assembly into nanotubes of viral capsid-like dimension. *Proc. Natl. Acad. Sci. U.S.A.* **100**, 10258–10262 (2003).
- C. Valéry, F. Artzner, M. Paternostre, Peptide nanotubes: Molecular organisations, self-assembly mechanisms and applications. *Soft Matter* **7**, 9583–9594 (2011).
- I. W. Hamley, Peptide nanotubes. *Angew. Chem. Int. Ed.* **53**, 6866–6881 (2014).
- U. B. Sleytr, P. Messner, Crystalline surface layers on bacteria. *Annu. Rev. Microbiol.* **37**, 311–339 (1983).
- J. M. Shively, F. Ball, D. H. Brown, R. E. Saunders, Functional organelles in prokaryotes: Polyhedral inclusions (carboxysomes) of *Thiobacillus neapolitanus*. *Science* **182**, 584–586 (1973).

14. C. A. Kerfeld, M. R. Sawaya, S. Tanaka, C. V. Nguyen, M. Phillips, M. Beeby, T. O. Yeates, Protein structures forming the shell of primitive bacterial organelles. *Science* **309**, 936–938 (2005).
15. S. Ganapathy, G. T. Oostergetel, P. K. Wawrzyniak, M. Reus, A. G. M. Chew, F. Buda, E. J. Boekema, D. A. Bryant, A. R. Holzwarth, H. J. M. de Groot, Alternating *syn-anti* bacteriochlorophylls form concentric helical nanotubes in chlorosomes. *Proc. Natl. Acad. Sci. U.S.A.* **106**, 8525–8530 (2009).
16. L. Jiang, Y. Peng, Y. Yan, J. Huang, Aqueous self-assembly of SDS@2 β -CD complexes: Lamellae and vesicles. *Soft Matter* **7**, 1726–1731 (2011).
17. L. Jiang, Y. Yan, J. Huang, Versatility of cyclodextrins in self-assembly systems of amphiphiles. *Adv. Colloid Interface Sci.* **169**, 13–25 (2011).
18. L. Jiang, J. W. J. de Folter, J. Huang, A. P. Philipse, W. K. Kegel, A. V. Petukhov, Helical colloidal sphere structures through thermo-reversible co-assembly with molecular microtubes. *Angew. Chem. Int. Ed.* **52**, 3364–3368 (2013).
19. S. Yang, Y. Yan, J. Huang, A. V. Petukhov, L. M. J. Kroon-Batenburg, M. Drechsler, C. Zhou, M. Tu, S. Granick, L. Jiang, Giant capsids from lattice self-assembly of cyclodextrin complexes. *Nat. Commun.* **8**, 15856 (2017).
20. S. Ouhajji, J. Landman, S. Prévost, L. Jiang, A. P. Philipse, A. V. Petukhov, In situ observation of self-assembly of sugars and surfactants from nanometres to microns. *Soft Matter* **13**, 2421–2425 (2017).
21. S. Kler, R. Asor, C. Li, A. Ginsburg, D. Harries, A. Oppenheim, A. Zlotnick, U. Raviv, RNA encapsidation by SV40-derived nanoparticles follows a rapid two-state mechanism. *J. Am. Chem. Soc.* **134**, 8823–8830 (2012).
22. G. Tresset, C. Le Coeur, J.-F. Bryche, M. Tatou, M. Zeghal, A. Charpilienne, D. Poncet, D. Constantin, S. Bressanelli, Norovirus capsid proteins self-assemble through biphasic kinetics via long-lived state-like intermediates. *J. Am. Chem. Soc.* **135**, 15373–15381 (2013).
23. I. Livsey, Neutron scattering from concentric cylinders. Intraparticle interference function and radius of gyration. *J. Chem. Soc. Faraday Trans.* **83**, 1445–1452 (1987).
24. D. Duchene, D. Wouessidjewe, Industrial uses of cyclodextrins and their derivatives. *J. Coord. Chem.* **27**, 223–236 (1992).
25. T. M. Weiss, T. Narayanan, C. Wolf, M. Gradzielski, P. Panine, S. Finet, W. I. Helsby, Dynamics of the self-assembly of unilamellar vesicles. *Phys. Rev. Lett.* **94**, 038303 (2005).
26. K. Bressel, M. Muthig, S. Prevost, J. Gummel, T. Narayanan, M. Gradzielski, Shaping vesicles—controlling size and stability by admixture of amphiphilic copolymer. *ACS Nano* **6**, 5858–5865 (2012).
27. E. Paineau, M.-E. M. Krapf, M.-S. Amara, N. V. Matskova, I. Dozov, S. Rouzière, A. Thill, P. Launois, P. Davidson, A liquid-crystalline hexagonal columnar phase in highly-dilute suspensions of imogolite nanotubes. *Nat. Commun.* **7**, 10271 (2016).
28. O. Glatzer O. Kratky, *Small Angle X-Ray Scattering* (Academic Press, 1982).
29. M. Volmer, A. Weber, Keimbildung in übersättigten Gebilden. *Z. Phys. Chem.* **119U**, 277–301 (1926).
30. R. Becker, W. Döring, Kinetische Behandlung der Keimbildung in übersättigten Dämpfen. *Ann. Phys.* **416**, 719–752 (1935).
31. J. Frenkel, A general theory of heterophase fluctuations and pretransition phenomena. *J. Chem. Phys.* **7**, 538 (1939).
32. D. Andelman, in *Handbook of Biological Physics*, R. Lipowsky, E. Sackmann, Eds. (Elsevier Science B.V., 1995), vol. 1, pp. 603–641.
33. J. Israelachvili, *Intermolecular and Surface Forces* (Elsevier, ed. 3, 2011), p. 291.
34. T. Dvir, L. Fink, R. Asor, Y. Schilt, A. Steinar, U. Raviv, Charged membranes under confinement induced by polymer-, salt-, or ionic liquid solutions. *Soft Matter* **9**, 10640 (2013).
35. W. Helfrich, R.-M. Servuss, Undulations, steric interaction and cohesion of fluid membranes. *Il Nuovo Cimento D* **3**, 137–151 (1984).
36. A. P. Philipse, B. W. M. Kuipers, A. Vrij, Algebraic repulsions between charged planes with strongly overlapping electrical double layers. *Langmuir* **29**, 2859–2870 (2013).
37. A. P. Philipse, R. Tuinier, B. W. M. Kuipers, A. Vrij, M. Vis, On the repulsive interaction between strongly overlapping double layers of charge-regulated surfaces. *Colloid Interface Sci. Commun.* **21**, 10–14 (2017).
38. P. Van Vaerenberg, J. Léonardon, M. Sztucki, P. Boesecke, J. Gorini, L. Claustre, F. Sever, J. Morse, T. Narayanan, An upgrade beamline for combined wide, small and ultra small-angle x-ray scattering at the ESRF. *AIP Conf. Proc.* **1741**, 030034 (2016).
39. M. Borsboom, W. Bras, I. Cerjak, D. Detollenaere, D. Glastra van Loon, P. Goettkindt, M. Konijnenburg, P. Lassing, Y. K. Levine, B. Munneke, M. Oversluizen, The Dutch-Belgian beamline at the ESRF. *J. Synchrotron Radiat.* **5**, 518–520 (1998).
40. T. Narayanan, J. Gummel, M. Gradzielski, *Advances in Planar Lipid Bilayers and Liposomes* (Elsevier Ltd., ed. 1, 2014), vol. 20, pp. 171–196.
41. F. Nallet, R. Laversanne, D. Roux, Modelling x-ray or neutron scattering spectra of lyotropic lamellar phases: Interplay between form and structure factors. *J. Phys. II* **3**, 487–502 (1993).

Acknowledgments: We thank P. Bösecke, D. Pontoni, P. Lloria, D. Hermida-Merino, C. Fernández-Rico, and J. Dominguez Pardo for their help during the measurements. **Funding:** J.L. and S.O. acknowledge financial support from the Netherlands Organisation for Scientific Research (grants 022.004.016 and 712.014.002, respectively). J.L. also acknowledges financial support from the ESRF. J.G. acknowledges financial support from Guangdong Innovative Research Team Program No. 2011D039. We also thank the Netherlands Organisation for Scientific Research and the ESRF for beamtime allocation on DUBBLE, ID02, and the Partnership for Soft Condensed Matter (PSCM) support. **Author contributions:** J.L., A.V.P., and T.N. designed the research. J.L., S.O., and A.V.P. performed experiments. S.P. and T.N. advised on experiment and data analysis. J.L. performed data analysis. J.G., A.P.P., and W.K.K. advised on theoretical models. J.L. developed the theoretical models. J.L. wrote the paper. All authors contributed to paper revision and critical reading. A.V.P. supervised the research. **Competing interests:** The authors declare that they have no competing interests. **Data and materials availability:** All data needed to evaluate the conclusions in the paper are present in the paper and/or the Supplementary Materials. Additional data related to this paper may be requested from the authors.

Submitted 1 February 2018

Accepted 17 May 2018

Published 29 June 2018

10.1126/sciadv.aat1817

Citation: J. Landman, S. Ouhajji, S. Prévost, T. Narayanan, J. Groenewold, A. P. Philipse, W. K. Kegel, A. V. Petukhov, Inward growth by nucleation: Multiscale self-assembly of ordered membranes. *Sci. Adv.* **4**, eaat1817 (2018).

Inward growth by nucleation: Multiscale self-assembly of ordered membranes

Jasper Landman, Samia Ouhajji, Sylvain Prévost, Theyencheri Narayanan, Jan Groenewold, Albert P. Philipse, Willem K. Kegel and Andrei V. Petukhov

Sci Adv 4 (6), eaat1817.
DOI: 10.1126/sciadv.aat1817

ARTICLE TOOLS

<http://advances.sciencemag.org/content/4/6/eaat1817>

SUPPLEMENTARY MATERIALS

<http://advances.sciencemag.org/content/suppl/2018/06/25/4.6.eaat1817.DC1>

REFERENCES

This article cites 35 articles, 5 of which you can access for free
<http://advances.sciencemag.org/content/4/6/eaat1817#BIBL>

PERMISSIONS

<http://www.sciencemag.org/help/reprints-and-permissions>

Use of this article is subject to the [Terms of Service](#)

Science Advances (ISSN 2375-2548) is published by the American Association for the Advancement of Science, 1200 New York Avenue NW, Washington, DC 20005. 2017 © The Authors, some rights reserved; exclusive licensee American Association for the Advancement of Science. No claim to original U.S. Government Works. The title *Science Advances* is a registered trademark of AAAS.